Optimization of mechanical properties of robocast alumina parts through control of the paste rheology

Mathilde Maillard, Jérôme Chevalier, Laurent Gremillard, Guilhem Baeza, Edwin-Joffrey Courtial, Sarah Marion, Vincent Garnier

Optimization of mechanical properties of robocast alumina parts through control of the paste rheology

Published in Journal of the European Ceramic Society 43[7] pp. 2805-17 (202)
https://doi.org/10.1016/j.jeurceramsoc.2022.12.008

M. Mailard[a], J. Chevalier[a,*], L. Gremillard[a], G.P. Baeza[a], E-J Courtial[b], S. Marion[a], V. Garnier[a]

[a] Univ Lyon, INSA-Lyon, CNRS, MATEIS UMR5510, 7 Av. Jean Capelle, F-69621 Villeurbanne, France.
[b] Univ Lyon, Université Lyon1, CNRS, CPE-Lyon, ICBMS, UMR 5246, 69622 Villeurbanne, France

* Corresponding author: Jerome.chevalier@insa-lyon.fr

Keywords
Additive manufacturing; Robocasting; Rheology; Strength; Fracture

Abstract
Robocasting, or Direct Ink Writing, can be used to create dense mono- or multi-materials ceramic parts using micro-extrusion of ceramic pastes through needles, whose position is controlled in 3D. Rheological properties of the ceramic pastes, printing parameters and thermal post processes (drying, debinding and sintering) are key parameters to control the quality of the printed parts. In this work, the rheological properties (including yield stress, shear-thinning behavior, storage/loss moduli and recovery time) of alumina pastes were characterized. Correlations were established between on one side the rheological properties and the printing conditions and on the other side the extrudability, the shape fidelity and the mechanical performance of the final parts. This paper thus defines an extended definition of printability, which includes functional requirements of the final parts in addition to the more classical processability criteria.

1. Introduction

Owing to its development in many domains, Additive Manufacturing (AM) of ceramics is becoming a key technology with a constantly growing market share [1]. Robocasting, also called Direct Ink Writing (DIW), is one of the AM technologies enabling to build mono or multi-material ceramics layer by layer [2-7]. It consists in the continuous extrusion of a ceramic paste through a thin nozzle (generally 0.2–0.9 mm), the position of which is controlled in 3D. The extruded material is designated by different names in the literature (paste, ink, feedstock…); the term 'paste' will mostly be used throughout the present article. The robocasting process starts with the definition of a Computer

Assisted Design (CAD) model. The design is then sliced, this step providing a definition of the nozzle path. The choice of an adequate slicing software is very important in order to minimize printing defects specially at the surface of printed part [8], as evidenced by Gleadall et al. who have shown the importance and the link between the success of the printing process and the software itself [9,10].

Although its general concept is rather simple, the success of robocasting requires ceramic pastes with specific rheological properties and appropriate processing parameters. In simple words, a ceramic paste is a mixture of a ceramic powder, organic components (binder, dispersant, and gelling agent) and a liquid carrier medium (mostly water). Non-Newtonian shear-thinning behavior is required in order to let the material, originally 'solid' in the syringe, become 'liquid' under shear stresses (generated by the shape of the nozzle and the printing speed) to flow through the nozzle [11,12]. This physical phenomena is possible due to the reorganization of particles and polymers under shear stress. To describe this behavior, the Ostwald-de Waele's relation is often proposed [13]:

$$\tau = k(\dot{\gamma})^n \qquad \text{(Eq. 1)}$$

τ and $\dot{\gamma}$ are the shear stress and strain rate respectively, where k is constant and n represents the difference with a Newtonian behavior ($n = 1$ for a Newtonian fluid). The apparent viscosity is then defined as $\eta = k\dot{\gamma}^{n-1}$. Shear-thinning is observed when $n < 1$, due to the decrease of viscosity under rising stress. A refinement of Eq. (1) is generally proposed on the basis of the Herschel-Bulkley equation (Eq. (2)), which includes a yield stress [13]:

$$\tau = \tau_y + k(\dot{\gamma})^n \qquad \text{(Eq. 2)}$$

Indeed, the process of extrusion requires an elastic shape retention of the paste after extrusion [14]. This translates into sufficient yield stress and elastic modulus (often called stiffness) to avoid layers collapse, guarantee a good stability and thus the desired shape and dimensions [15].

Defining viscosity and yield stress are first steps to characterize ceramic pastes, but a necessary step further consists of defining the overall viscoelastic behavior, often characterized through oscillatory measurements and resulting into the definition of a complex shear modulus (G*) such as [16]:

$$G^*(\omega) = G'(\omega) + iG''(\omega) \qquad \text{(Eq. 3)}$$

In the above expression, $G'$and G'' are called the storage and loss moduli, respectively assigned to the in-phase ($\varphi = 0$) and out-of-phase ($\varphi = \frac{\pi}{2}$) responses of the viscoelastic material, ω is the angular frequency. The complex viscosity η* can be derived from these data using:

$$|\eta^*| = |\eta' + i\eta''| = \frac{\sqrt{G'^2 + G''^2}}{\omega} \qquad \text{(Eq. 4)}$$

While G' represents the elasticity of the material, i.e., its 'solid-like' behavior, G'' represents the dissipated energy, i.e., its 'liquid-like' behavior. Therefore, the G''/G' ratio, often expressed as a function of the phase shift between the stress and the strain, tan (δ), gives a relative indication on the fluidity of the material: G''/G' < 1 characterizes a 'solid-like' behavior, whereas G''/G' > 1 characterizes a 'liquid-like' material [17]. The stress for which G'=G'' is often called flow stress, τ_f.

To determine these moduli, oscillatory rheology is performed. This rheological evaluation leads to the evolution of G' and G'' as a function of several variables such as the strain amplitude, the frequency of the solicitation, the time or even the temperature. Amplitude tests (or dynamic strain sweep) give access to the stiffness of the paste, which is defined as the constant G' value observed in

the Linear Viscoeslatic Region (LVR), before it decreases with strain amplitude. This value is often called G'_{eq} [18].

All these rheological studies are widely used in bioprinting literature [19-22] and start to pervade in the field of ceramics [23]. If aims of rheological studies in bioprinting are for example to study cells survival in the hydrogel during the printing process [24,25], for ceramic science, attention must be given to the absence of printed defects to reach sufficient mechanical properties [26-28].The concept of 'printability' is something very complex and strongly related to the additive manufacturing process itself and the final properties targeted. Lot of authors gave some criteria in order to optimize entire printing processes from formulation to printing parameters. Those criteria are still discussed and need to be completed [29].

At this stage, it is important to define exactly how the yield stress is precisely obtained. Generally, it is described as the stress needed to make the fluid start or stop moving and it usually defines the highest stress where no flow is detected by the rheometer [30-32]. In fact, according to rheological definitions and general literature, three different yield stresses could be defined:

1. the static yield stress (τ_γ^{STAT} or σ_γ^{STAT}), which corresponds to the shear stress necessary to initiate a flow when increasing the shear stress.
2. the dynamic yield stress (τ_γ^{DYN} *or* σ_γ^{DYN}), which is the minimal stress required to maintain the flow when decreasing the shear stress from the 'liquid-like state'.
3. and, to finish, the flow stress (τ_f or σ_f), which is the stress for which G'=G''.

In addition to the conventionally used yield stress(es) τ_γ and viscosity η, the use of extended rheology measurements and complex shear modulus enables the definition of other criteria of interest as 'figures of merit' of ceramic pastes. For example, to ensure a minimal deformation of overhanging structures and a suitable extrudability, Lewis et al. proposed that the ratio ϕ ($G'_{eq}/\ \tau_\gamma$) should be higher than 20. Another quantitative criterion from amplitude sweep corresponding to the ratio of yield stress and the flow stress, called 'FTI' for Flow Transition Index (it should be lower than 20), is commonly used to described 'printability' of paste [33], [34]. This criterion, though, could not display a clear trend according to Corker et al. [29]. To account for possible slumping of the printing structures due to both gravity and surface tension, Smay et al. determined that the dynamic yield stress should be higher than the sum of the gravity forces, leading to the criterion $h_{max} = \frac{\tau_\gamma^{DYN}}{\rho g}$ [19,35] (h_{max} is thus the maximum possible printable height with a given paste) [35]. This obvious and physically grounded criterion can also be improved by taking into account the surface tension of the printed material, thus becoming: $\Xi = \frac{\tau_\gamma^{DYN}}{\rho g h + \gamma R^{-1}}$ ($\Xi > 1$ is necessary to ensure shape retention after printing).

Another important, although somewhat 'under-emphasized', effect in viscoelastic material is thixotropy, which corresponds to a time-dependent shear-thinning property [36,37]. In practical terms, the viscosity of a thixotropic material not only depends on stress and strain rate, but also on time and shear history. Due to this time-dependence, when loading a paste first at high strain rate, then at lower (e.g. zero) strain rate, a stress relaxation will occur. This relaxation is related to time-dependent microstructural evolutions ('healing') of the paste to come back to its original state. The time required to obtain a new viscosity similar to the original one is called 'recovery time' (or healing time) and has to be considered in order to choose the size of the printed part.

All the rheological requirements presented above are summarized in Fig. 1. Although these rheological properties are essential to ensure a good extrusion of the paste and no collapsing of the printed structure during the printing process, they do not fully ensure good performances of the final part (porosity, inter-filaments defects, surface state, and thus mechanical properties are not addressed by the above-mentioned criteria). Indeed, the quality of the printed part will depend on three families

of parameters. First, similarly to all other ceramic processes, composition of pastes and their homogeneity are important factors to guarantee the least possible defects. For example, increasing the volume fraction of ceramic particles will lead to rheological modifications which could be harmful for a safe homogeneity during all the process. Second, environmental parameters, such as temperature and humidity, are also essential to avoid cracks during the printing process. The homogeneity of the filament can be mainly maintained under high humidity to avoid cracks due to too rapid drying [38-40]. Third, the choice of printing parameters will influence shape fidelity and final geometries, so indirectly, final properties: for example, printing speed will influence the overall aspect of the printing filament and its shape [41,42]; the degree of overlap and size of the nozzle will influence the shape fidelity of ceramics due to the topography of the printed part related to layer stacking.

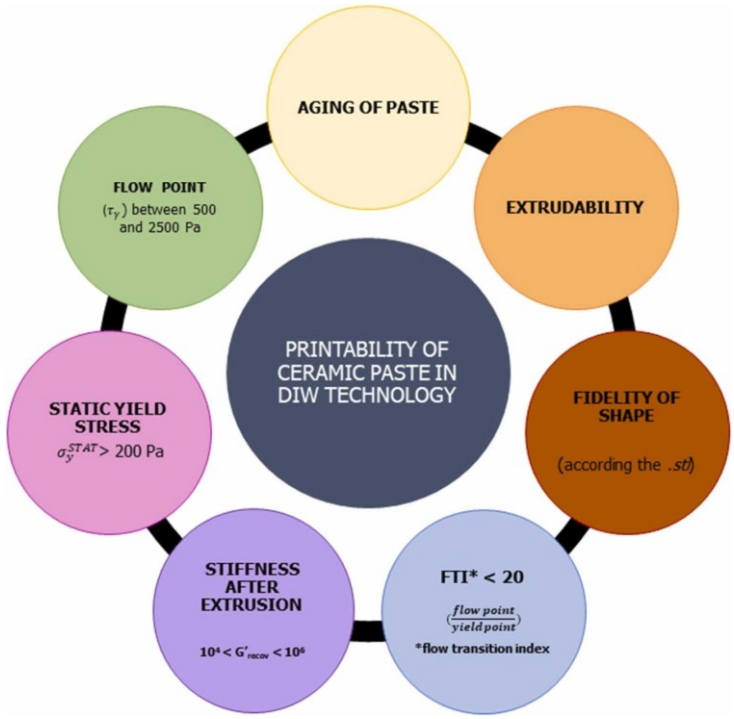

Figure 1: Rheological requirements in DIW process [5,22,23,29,33,43].

Finally, following printing, thermal treatments are necessary, first to dry the printed parts, then to debind and sinter them. These treatments will also influence the final properties, since they can induce defects such as drying cracks or distortions due to non-homogeneous shrinkage. All this post-printing step will thus influence the final functional (mechanical) properties [44-47].

In this article, a multi-criteria approach to obtain printed ceramics with good shape and mechanical properties is emphasized. DIW technology was used to fabricate dense alumina pieces with two geometries (dense bars and hollow tubes). The influence of the rheology of the pastes at all steps of the process was evaluated. The rheology of the pastes was modified by varying the solids loading, nature and amount of the gelling agent and amount of the dispersing agent. Finally, mechanical strength of printed parts was measured. This work examines the correlations between all these parameters in order to extend the definition of "printability" beyond rheological properties only.

2. Materials and methods

2.1. Raw materials

Pluronic® F-127 (polyethylene oxide – polypropylene oxide – polyethylene oxide triblock copolymer, referred to as PF127) and Poly-Ethylene Glycol (PEG with molecular weight 4,000 $g.mol^{-1}$ and 20,000 $g.mol^{-1}$ respectively called hereafter PEG4000 and PEG20000) were purchased from Sigma

Aldrich (Saint-Quentin-Fallavier, France) and used without further purification. A sodium polyacrylate (Darvan® 811, RT Vanderbilt, Norwalk, USA) was used as dispersing agent. The Alpha-alumina ceramic powder was provided by Baikowski (Poisy, France); it was a Baikalox® High Purity Alumina WA15 powder, with a specific surface area of 23.6 m^2/g and a D50 of 0.15 µm. Milling balls (mixture of 2 mm diameter alumina balls and zirconia (Mg-PSZ) balls) were used to facilitate the homogenization of the pastes.

2.2 Ceramic pastes preparation

Pastes based on 2 different gelling agents (PF127 +PEG4000 or PEG20000) were prepared following identical steps. The first step was the preparation of the polymeric solution.

In the case of the PF127-based pastes, PF127 solutions at 20% w/v (20 g in 100 cm^{-3} of water) were prepared by mixing adequate amounts of PF127 powder and deionized water at 4 °C with a magnetic stirrer. The solution was then mixed with cycle at 2000 rpm for 2 min using a Speedmixer (Hauschild GmbH & Co.KG, Hamm, Germany) and stored at 0 °C for 24 h. In parallel, a PEG 4000 aqueous solution at 3% w/v was prepared by stirring PEG4000 powder with water using a magnetic stirrer, at 55–60 °C. After cooling, the PEG4000 solution was added to PF127 solution.

In the case of the PEG20000-based pastes, PEG solutions at 20% w/v and 10% w/v (with the PEG20000) were prepared by stirring PEG powder with water at 55–60 °C. Solutions were then mixed at 2000 rpm for 2 min using the Speedmixer and stored at 0 °C for 24 h.

Then the preparation steps were common for all pastes:
1. Addition of the dispersing agent (Darvan® 811)
2. Addition of the mixing balls (same weight as the ceramic powder)
3. Addition of the alumina powder, in two steps in order to optimize the dispersion of the powder and the homogenization of the paste. After each addition the mixture was homogenized in the Speedmixer (4 cycles of 1 min at 1500–1850 rpm, with 2 min cooling in an ice bath between each cycle).

Four pastes were selected from a prior preliminary study to focus on the most demonstrative effects. Two of them were based on PF127 20% w/v solution and contain 38 or 42 vol% alumina powder. They are labeled respectively ADP38 and ADP42. A third paste was based on a 10% w/v PEG20000 solution and contained 38 vol% alumina. It is labeled ADPeg38. The last paste (labeled ADPeg38_20) was based on a 20% w/v PEG20000 solution and also contained 38 vol% alumina. The compositions of the pastes are detailed in Table (1).

Table 1. Composition of the alumina pastes.

Name of the paste	Alumina (g)	Solution of PF127 20% w/v (g)	Solution of PEG 4000 at 3% w/v (g)	Solution of PEG 20,000 10% w/v (g)	Solution of PEG 20,000 20% w/v (g)	Darvan 811 (g)
ADP38	40	16.06	1.200			0.200
ADP42	40	13.34	1.200			0.360
ADPeg38	40			19.55		0.300
ADPeg38–20	40				19.55	0.300

2.3 Rheological properties

For each ceramic paste, the following rheological tests were carried out using an ARES strain-controlled rheometer (Rheometrics instruments, USA) equipped with 2kFRTN1 transducer. The geometry used was a 25 mm cone-plane geometry with a cone angle of 0.1 rad and 0.05 mm gap. Measurement was performed keeping a constant temperature of 21 °C. The different rheological tests performed could be segmented into 3 categories:

- Oscillatory strain sweeps (controlled shear deformation) allow to determine the (non-destructive) deformation of the pastes at small strains and study the behavior in the Linear Visco-Elastic Region (LVER), through the evolution of storage and loss moduli (G' and G'') versus strain amplitude. They were conducted at a constant angular frequency of 10 rad/s, on three decades of deformation (0.1–100%). Value of the flow point τ_f, static yield stress τ_γ and limits of the LVER were obtained.
- Oscillatory frequency sweeps allow to describe the viscoelastic behavior of the pastes as a function of the frequency. High frequency values are used to mimic fast deformation. Low frequency values will mimic the 'steady' behavior in the syringe of the paste. Frequency sweep tests are ideal to study the internal microstructure and have an idea about the stability of the paste with time. These tests involved a frequency ramp from 0.01 to 100 rad/s, at a constant stress of 0.1 kPa (selected in agreement with the previous results, to remain on the plateau zone of G') in order to determine tan(δ) and the viscoelastic behavior of the pastes.
- Start-Up tests were conducted in order to determine the recovery time and the thixotropic behavior of formulation. They consisted in the measurement of the evolutions of the storage modulus and viscosity with time under three successive conditions: (1) a pre-shear of 3 s^{-1} for 120 s (to characterize the paste before extrusion), (2) a high shear-strain rate of 60 s^{-1} for 10 s (mimicking the extrusion) and (3) a shear rate of 3 s^{-1} during 500 s. The recovery time corresponds to the time needed for the paste to recover a stiffness or a viscosity similar (for example 90%) to its initial value [48].
- All rheological parameters obtained from these different tests are summarized in Table (2).

Table 2. Definition of rheological properties.

G'	Elastic (or storage) modulus
G''	Viscous (or loss) modulus
η*	Complex viscosity
Tan(δ)	Loss factor (indication of the fluidity of the material)
LVER (G'_{eq}) often called G'_{LVER}	Linear Visco-Elastic Region at small strain (and related storage modulus) sometimes called stiffness
τ_γ (yield stress) often called σ_γ	Stress needed to leave the LVER
τ_f (flow point or flow stress) often called σ_f	Stress for which G'=G'', which is considered as the transition between a 'liquid-like' and a 'solid-like' paste
$t_{G'}$	Time needed to recover "high" viscosity or initial rigidity after the extrusion. Here $t_{G'}$ was defined as the time necessary to recover 90% of viscosity at rest (without shear).

2.4 Printing conditions

A Robocasting system (3D-Inks, Tulsa, USA) was used for all printings, controlled by the Robocad software, a graphical user interface designed to produce G-code interpretable by the printer. All the samples were printed with 0.410 mm diameter nozzles and the printing speed was fixed to 10 mm/s to obtain continuous filaments during the printing process. A layer height of 0.33 mm (corresponding to an overlap in the z-axis of 20% of the nozzle diameter) was chosen to allow good interpenetration of layers (and thus avoid large defects between filaments). With the same goal, a pitch of 0.4 mm was chosen (the pitch is the distance between the centers of two adjacent filaments).

Two types of samples were printed:

1. Bending bars with dimensions (l x w x h) of 36 ×4× 5 mm^3 (dimensions after printing) consisted of 15 layers. Each layer was printed lengthwise, and was shifted widthwise by a

filament half-diameter with respect to the previous layer to avoid longitudinal empty channels between each filament and obtain best final properties, in agreement with Feilden et al. [27].

2. Hollow cylinders (outer diameter, height, thickness after printing: 20 × 20× 1.2 mm3) were processed with a stack of 37 layers consisting of 3 filaments by layer. Each layer was printed directly on top of the previous one, without horizontal shift contrary to the bending bars, due to the small thickness of the structures.

2.5 Drying, debinding and sintering processes

Ceramics parts were dried in a climatic chamber (WKL 150 Weiss Technik, France). At first the samples were put in the climate chamber (25 °C and 98% HR) and the relative humidity kept constant at 98% HR while temperature was increased up to 60 °C during 1.5 h. Then the relative humidity was decreased to 30% in about 4 days while the temperature was maintained at 60 °C.

The debinding process consisted in a slow heating (0.5 °C/min) followed by a 30 min dwell at 400 °C, then a 1 °C/min heating to 600 °C with a 30 min dwell, followed by natural cooling. Sintering was conducted at 1500 °C with a 1-hour dwell (5 °C/min heating rate, natural cooling).

2.6 Solid state mechanical properties

Mechanical tests were performed with an INSTRON 8800 universal testing machine (Norwood, USA) with a 5 kN load-cell, at room temperature.

Four-point bending tests were conducted on as-sintered samples (i.e. without surface grinding nor polishing, in order to characterize the real surface state of components after 3D printing), at a cross-head speed of 0.5 mm/min with a support span L (mm) of 21 mm and inner span L' of 10 mm.

The flexural strength σ_f(MPa) was obtained by:

$$\sigma_f = \frac{3}{2} F_M \left(\frac{L-L'}{BW^2}\right) \qquad \text{(Eq. 5)}$$

where F_M is the load to failure, B and W the width and the height of sample respectively (measured after sintering on each sample).

Tubes were tested using a diametral flexural strength configuration. They were positioned with the printing origin at 45° with respect to the testing direction, so that the printing origin is not on a location where the stress is maximal. The strength was derived from the load to failure by the equation [49]:

$$\sigma_f = 2F_M r \left(\frac{6r-t}{\pi l t^2 (2r-t)}\right) \qquad \text{(Eq. 6)}$$

Where t is the wall thickness, r the mean radius, l is the length and F_M is the fracture load.

Finally, Weibull moduli were deduced from the 4-point bending strengths, using two-parameters Weibull expression:

$$P_f = 1 - exp\left(-\left(\frac{\sigma}{\sigma_0}\right)^m\right) \qquad \text{(Eq. 7)}$$

where P_f is the probability of failure at applied stress σ, σ_0 the characteristic strength for which the probability of failure is 63% and m is the Weibull modulus, which gives an indication of failure distribution (low m value meaning a large variability). A careful and precise Weibull modulus analysis requires numerous specimens to be tested (typically more than 30, according to the ISO standards and according to literature [50]). As we were limited to 10 (hollow structures) to 18 samples (bars), Weibull moduli obtained are given as indications only and will be associated to a confidence interval. A 95% confidence interval was given for both the characteristic strength and the Weibull modulus, following the work of Davies [50].

2.7 Microstructural characterization

Densities of printed part were evaluated after sintering by the Archimedes method. Macroporosity assessments were also conducted by SEM analysis. Microstructures were characterized by Scanning Electron Microscopy (SEM) using a Supra40VP microscope (Zeiss, Oberkochen, Germany). Fracture surfaces of selected samples were analysed according to Morrell [51] in order to determine the fracture origin.

3. Results

3.1. Viscoelastic properties and Linear domains of the ceramic pastes

Results of oscillatory strain sweep tests are illustrated in Fig. (2). They confirm the influence of solids loadings in four formulations: ADP38, ADP42, ADPeg38 and ADPeg38_20 and show their rheological behavior. PF127 (20%w/v) itself was also evaluated and showed much lower stiffness. All pastes, and PF127 alone are, as expected, (typical) viscoelastic materials with a decrease of *G'* with strain and a crossover between *G'* and *G''* (from 'solid-like' to 'liquid-like'). Due to its small molecular weight, the addition of PEG4000 into PF127 solution did not lead to a significant modification of rheological properties which explains the choice to not show this result.

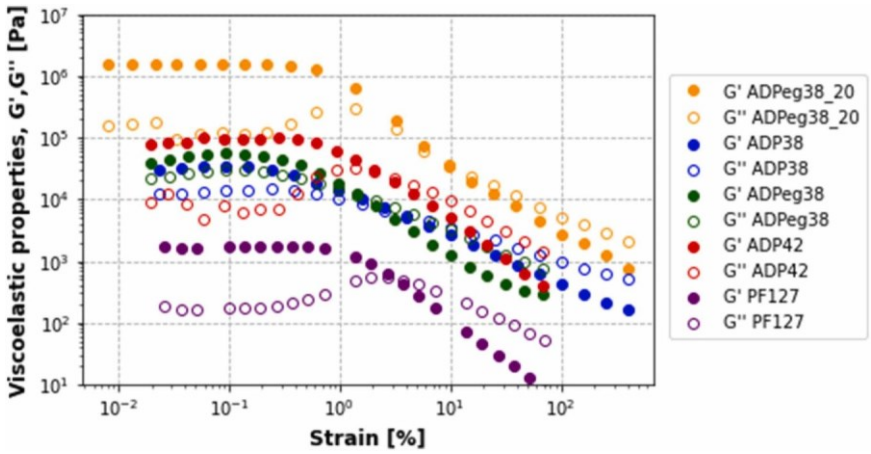

Figure 2. Viscoelastic properties (storage modulus G' and loss modulus G'') of four formulations and PF127 20% w/v by oscillatory rheology (strain sweep).

Fig. 2 also shows the presence of a LVER (areas where G' is a constant before starting to decrease) for all pastes. These areas are more or less extended according to the composition of the paste. ADPeg38_20 showed the highest G'_{eq}, larger than 10^6 MPa. This is a too high stiffness for DIW, thus ADPeg38_20 was not studied further. ADP42 paste showed the second largest LVER. It also exhibited a high stiffness, with G'_{eq} around 110 kPa, while ADP38 and ADPeg38 were around 30 kPa and 20 kPa respectively, which (if recovered after extrusion) would be sufficient to ensure shape retention.

The stiffness of a paste logically increases with the addition of ceramic particles. However, G'- G'' crossover is always visible, which confirms that the viscoelastic behavior required for DIW was obtained for all pastes. Under oscillatory strain sweep tests, ADPeg38 shows a behavior quite similar to ADP38 paste, while containing less organic compounds (to release during debinding) and being less sensitive to temperature.

3.2 Flow behavior

Fig. 3 represents the evolution of tan(δ) and of the complex viscosity (η*) of the three remaining pastes as a function of the angular frequency, when staying in the LVER. Logically, tan(δ) is close to zero for low frequency, indicating a large value of G' compared to G''. Over the whole frequency domain scanned here and for the selected shear stress of 0.1 kPa, tan(δ) < 1 for the three pastes, which characterizes a solid-like behavior and could be assimilated to a tri-dimensional network. The 3 pastes

show complex viscosity decreasing with frequency which confirms the shear-thinning behavior. Interestingly, the evolutions of complex viscosity with angular frequency of ADP38 and ADPeg38 are quite similar.

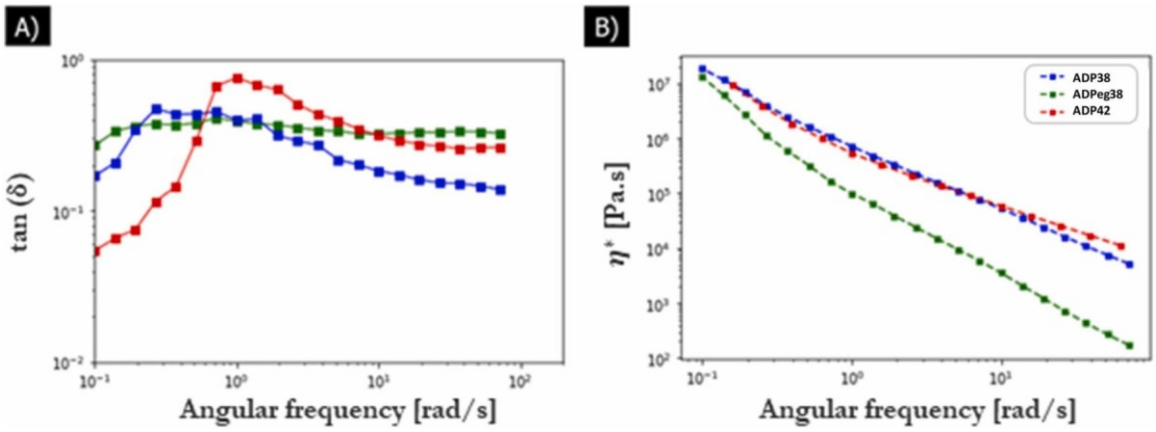

Figure 3. Solid-like and shear-thinning behavior of alumina pastes: Evaluation of tan (δ) and viscosity in function of angular frequency in dynamic frequency sweep. Shear viscosity curves.

3.3. Yield stress and flow points

Fig. 4 shows static yield stresses (τ_γ) and the flow stresses (τ_f) of the 3 pastes, obtained in dynamic strain sweep (G',G" versus oscillation stress) curves. Yield stresses values are determined when storage modulus start to drop at the end of the linear domain. Values obtained for the ADP38, ADPeg38 and ADP42 are respectively 100 Pa, 200 Pa and 500 Pa. Flow stresses which are calculated at the crossover G'=G'' are 250 Pa, 300 Pa and 1000 Pa. The 'breaking' area (between yield point and yield stress) is lower for ADPeg38 and ADP42, which can be explained by the lower homogeneity in ADP42 and the difficulty to break the network.

Fig. 4D summarizes the different rheological parameters obtained for the 3 pastes and the 'figures of merit' defined in the literature. All three pastes can be considered as 'printable' according to these criteria. ADP38 and ADPeg38 are quite close, which is interesting in order to use a paste with less organic compound.

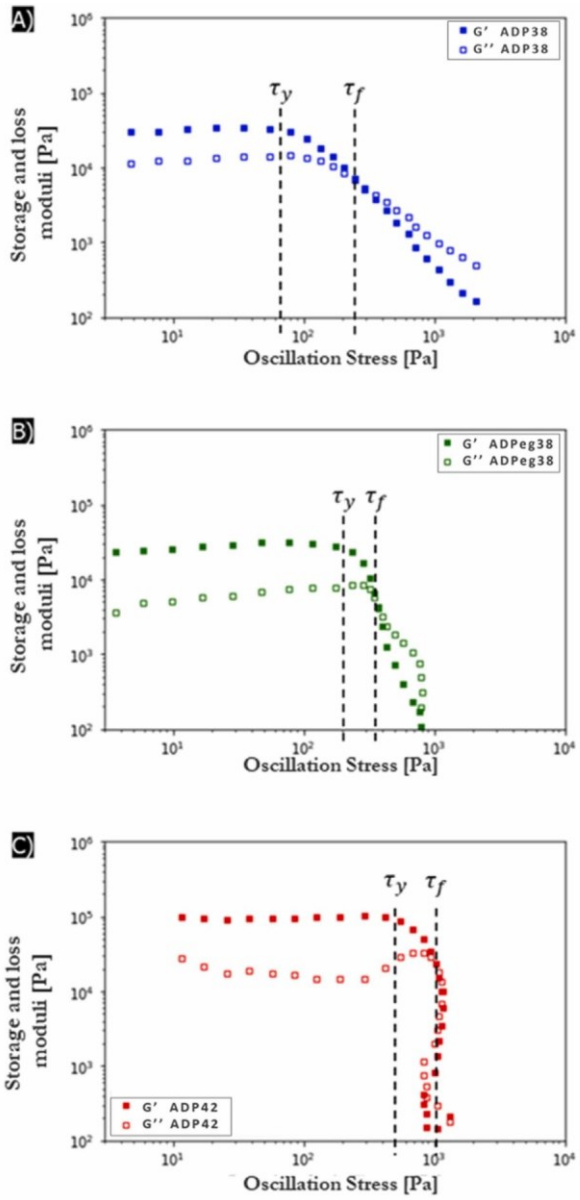

D)	*Stiffness G'_{eq} (Pa)*	*Yield stress τ_y (Pa)*	*Flow stress τ_f (Pa)*	*FTI (τ_f /τ_y)*	*Φ (G'_{eq}/ τ_f)*
Range required for 'printable' pastes	1.10^4 - 1.10^6	100 - 2500	100 - 2000	0 - 20	> 20
ADP38	3.10^4	100	250	2.5	113
ADP42	1.10^5	500	1000	1.8	110
ADPeg38	$4.5.10^4$	200	300	1.5	161

Figure 4. Flow stress (τf) and yield stress (τγ) of 3 pastes in dynamic strain sweep A) ADP38. B) ADPeg38. C) ADP42. D) summary of the measured values.

4. Solid state mechanical properties

4.1. Optimization of printing parameters

Defects which may appear in dense printed parts were studied before going towards final samples for testing. Typical defects that can be observed by SEM are illustrated in Fig. 5. Fig. 5A illustrates a bad homogeneity during the formulation process for ADP42 paste, due to a deficient amount of dispersing agent in relation to the volume fraction of alumina powder. Fig. 5B represents printed parts without enough overlap and pitch for ADP38 paste, thus without enough interpenetration of the neighboring filaments. Fig. 5C gives an example of a technology printing issue, with a lack of a layer in the G-Code which creates an hollow space after the first layer for ADP42 optimized paste. Fig. 5D illustrates an acceptable sample, with the optimized printing parameters but still a few remaining pores, due to

a bad homogeneity during the mixing process of materials. These few examples highlight the fact that optimal rheology of the paste is mandatory, but not enough to obtain samples with a low amount of (small) defects.

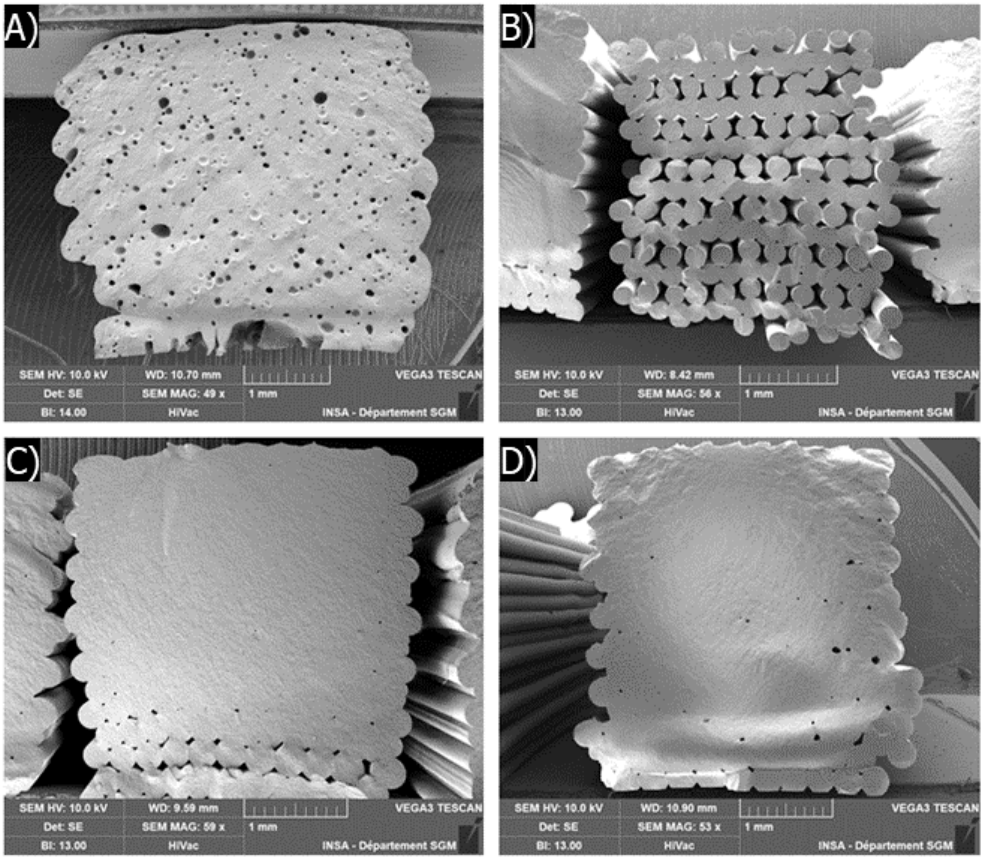

Figure 5. Illustrations of defects found with non-optimized conditions related to A) Bad homogeneity of the paste (ADP42 with a deficiency in Darvan 811 dispersant: the paste was so stiff that the bubbles could not be eliminated), B) Bad choices of overlap in y and z, C) First layr missing in the G-Code (optimized ADP42), D) Air bubbles trapped.

4.2. Strength of printed parts

Parts printed with ADP38 and ADPeg38 exhibited very similar relative densities after sintering (respectively 91 ± 4% and 90 ± 5%) but with a quite high variability (density ranging from 90% to 98% for ADP38 for example). However the average density of parts printed with ADP42 was 85 ± 11%: the paste with the highest amount of alumina resulted (by far) in the lowest density after sintering, with the highest variability. Thus, pastes with a too high stiffness and yield stress are 'printable' but give rise to porous structures with insufficient density.

Fig. 6 illustrates results from fracture tests performed on alumina (unpolished) printed parts with the 3 formulations, in the form of fracture probability versus applied stress curves. In the 4-points bending configuration, the ADP42 bars (printed from the past with the highest solids content) show the lowest strengths values (from 100 to 300 MPa), while the two other modalities show non-significant differences. This is in agreement with the low density of pieces obtained from the highly-loaded paste. The characteristic strength and Weibull modulus of the 4 types of samples are given in Table 3. The low Weibull moduli are also in agreement with the large density variability mentioned above. Overall, it is shown that the pastes should not be too stiff to obtain acceptable strength. It also shows that PEG can be a good substitute to Pluronic, since it gives, for half the amount of organics, a quite similar extrusion behavior and self-standing ability of the filaments, thus in turns similar strength properties. Last, strengths obtained in this work (σ0 of ADP38, ADPeg38 and ADP42 are respectively 350, 325 and 250 MPa) are significantly improved when compared to existing literature on DIW [52] and even comparable to the strength commercially available alumina ceramics, and this without post-process treatments like polishing.

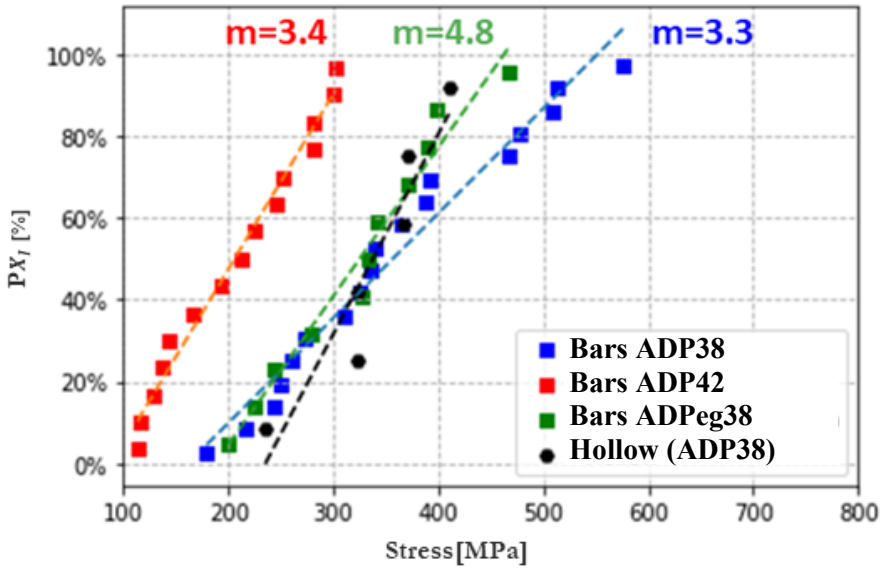

Figure 6. 4-point bending of alumina unpolished printed parts (bars and tubes) with 3 pastes: probability of failure versus stress.

Table 3. Strength and Weibull modulus distribution analysis.

Type of sample	*Characteristic strength σ_0 (MPa, 95% confidence interval)*	*Weibull modulus m (95% confidence interval)*
ADP38 (bars)	360–440	1.5–6
ADP42 (bars)	205–255	2.5–8
ADPeg38 (bars)	340–420	1.5–6
ADP38 (tubes)	340–420	*(too few samples)*

Interestingly, the diametral flexion fracture tests conducted on ADP38 tubes lead to σ_0 values very similar to the ones obtained in 4-points bending. This highlights the adequacy of this paste to print structures with complex shapes with thin walls, since the mechanical properties were independent of the testing configuration (which would need confirmation on a larger set of testing configurations). It is important to notice that the low Weibull moduli indicate a quite large heterogeneity in our result. In fact, these parts were printed during summertime which lead to thermosensitive issue due to the presence of PF127. PF127 pastes based become quickly tough during the printing which should have been created random defects. To finish, high strength values (like 500–600 MPa) could be explained by the absence of big defect due to the AM technology and the good homogeneity of ceramic paste. ISO 6872 standard [53] on ceramics for dentistry requires for example a flexural strength of 300 MPa for single crowns, which could thus be reachable with DIW and optimization of printing parameters and formulations.

4.3. Fracture surfaces of printed part

In order to determine the origin of the failure, fracture surfaces of samples tested in four-point bending were studied by SEM. Two examples of fracture surfaces for low strengths are illustrated in Fig. 7 in the green section. The yellow rectangle corresponds to first layers of each printed parts. At the top, a large crack, approximately 80 µm length, may have occurred during drying and debinding processes. The pictures at the bottom show another type of defects, which may be caused by a contamination and lead to generation of elongated Beta-alumina grains, likely linked to the presence of calcium or sodium [54,55]. These defects are between 80 and 100 µm in length and can be detrimental. They were rarely observed, but systematically led to low strength results.

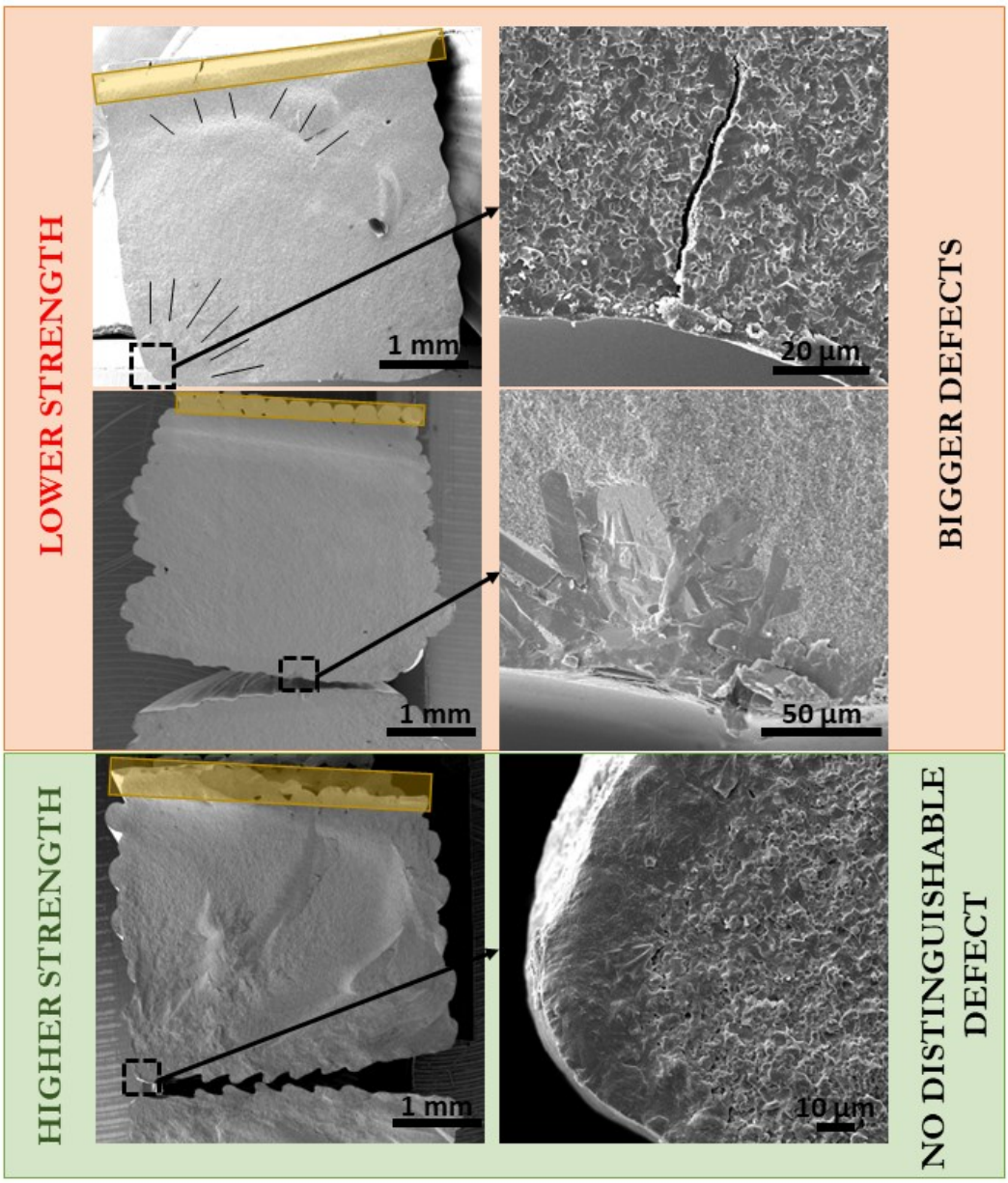

Figure 7. Analysis of defects in fracture surfaces of printed parts with lower strength (red) and higher strength (green).

Fracture surface of samples with higher strengths are also shown for comparison. The tensile faces show no distinguishable defect at low magnification. At higher magnification, a shell of 10 µm with a different surface roughness is observed. More important, the wavy surface of robocast samples is underlined, which by itself certainly plays on the strength of even the best samples.

4.4. Linking rheology and mechanical properties

Both the absence of major defects inside the parts and the fracture origins identified in Fig. 7 hint to the surface being one of the major limitations to obtain good mechanical properties. More detailed observations of the surface of printed parts, shown in Fig. 8, reveal a rougher surface for the samples printed with ADP42 (that presents the lowest strength and as a reminder the highest paste stiffness). Interestingly the two pastes with 38% solid content, although exhibiting quite similar values of stiffness and yield stress, lead to different surface states after printing. To evaluate how to smoothen the surface prior (or without) any polishing step, one could adjust the recovery time. Indeed, Fig. 9 shows that a shorter recovery time is measured for ADP38 than for ADPeg38 (few seconds for ADP38 to recover 90% of the initial viscosity and ~80 s for ADPeg38 to recover only 40% of the original viscosity). During this period, the lower viscosity allows the just-extruded filaments to flow slightly and thus present a smoother surface.

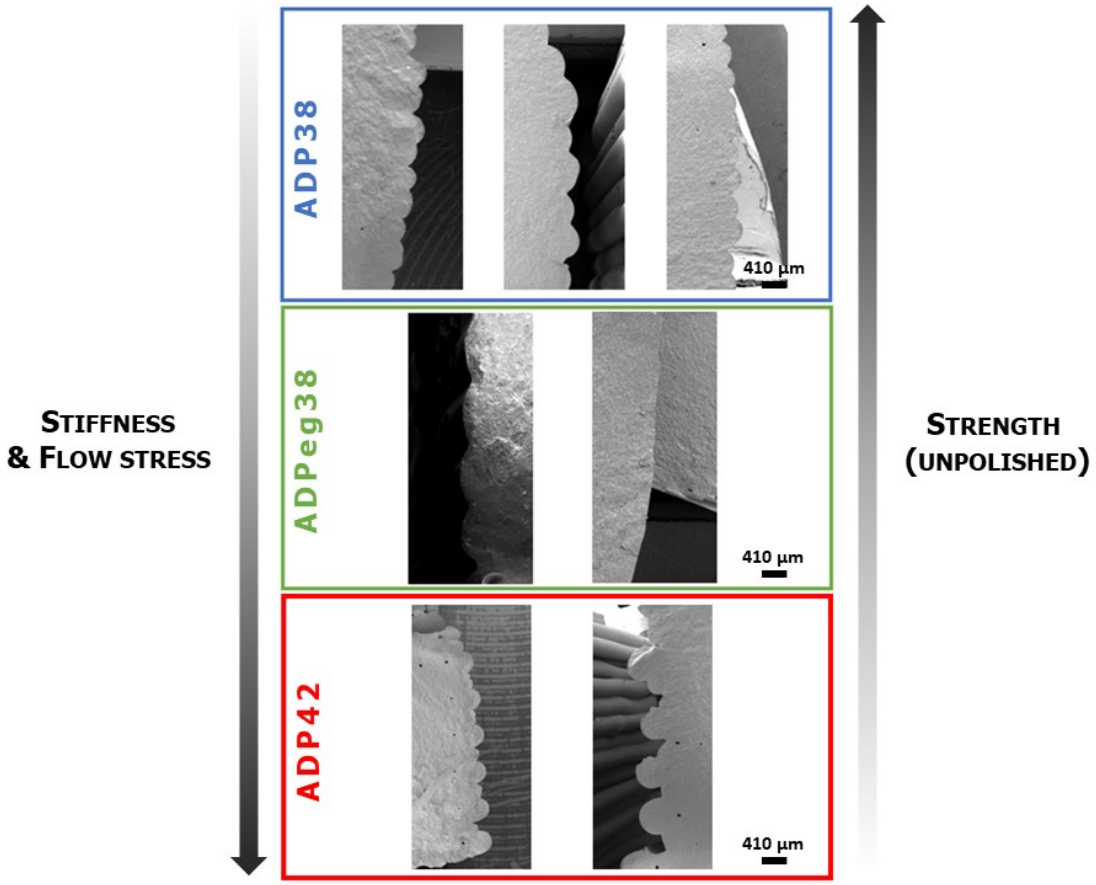

Figure 8. Topography analysis of three different formulations in relation to strength and rheological properties. ADP38 in blue and ADPeg38 in green show lower stiffness and higher strength, when ADP42 in red shows higher stiffness and lower strength. Note the surface state of ADP42 with a larger roughness.

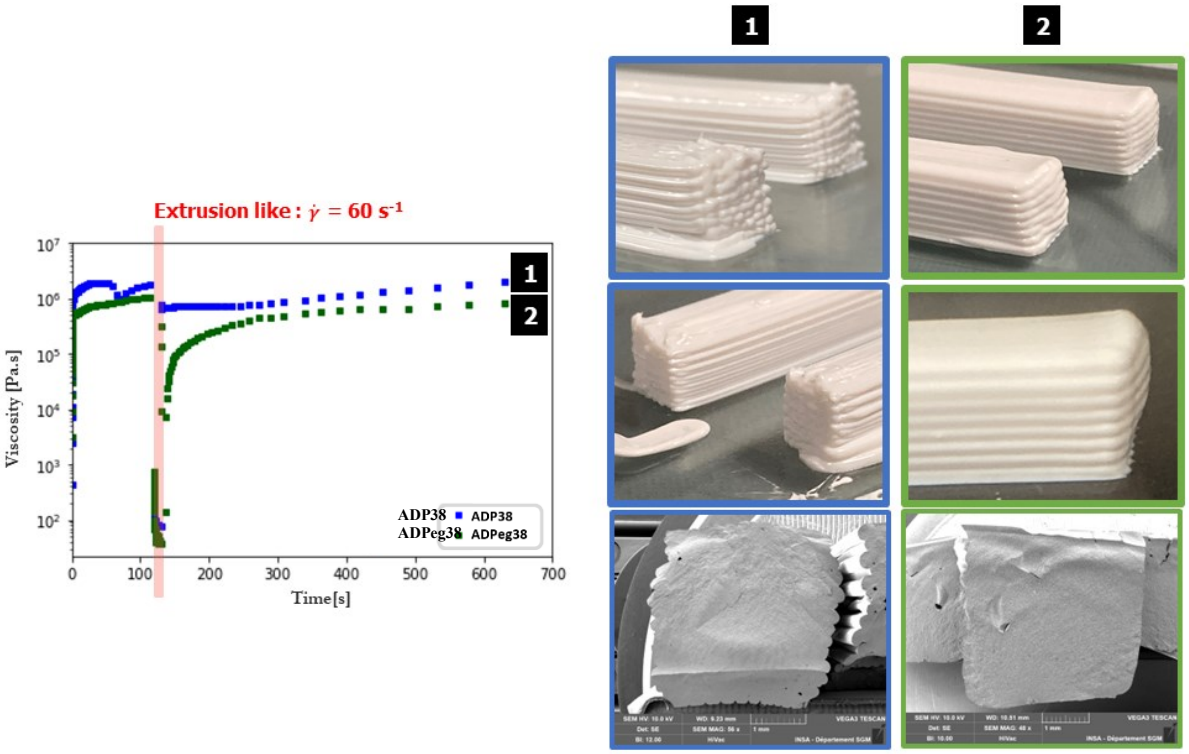

Figure 9. Start-up tests, performed on ADP38 (in blue) and ADPeg38 (in green). ADPeg38, with a longer healing time, shows a smoother surface.

5. Discussion

The rheology of the paste is a key property to ensure the printability of the paste. Since numerous rheological parameters are available, they can be combined in printability criteria. Fig. 4D summarizes the rheological characteristics of the 3 alumina pastes selected and two calculated criteria: Φ (G'eq/τ_γ) and FTI (Flow Transition Index). According to the literature, both these criteria could delimit a printability domain defined on a storage modulus versus apparent yield stress space. In the present work, all pastes are in the printability domain (FTI < 20 and Φ > 20). However, the printed parts exhibit different strength, illustrating the limitation of Φ and FTI: they will help to predict printability but not the final quality of the parts.

Besides the printability criteria, successful printing of a ceramic part implies knowing the necessary conditions of the process to obtain the part with adequate shape, both internally (architecture) or externally. Some of the printer-based parameters are essential for good shape fidelity. The pitch, overlap and printing speed parameters must be optimized to allow good overlap of the filaments in order to obtain a completely filled body (when dense parts are desired as it is the case here). Rheological parameters can also help in obtaining a good shape fidelity. For example, an adequate recovery time may allow the filaments to better overlap each other prior to the re-augmentation of the storage. The recovery time is thus significant to print parts with smooth surface and dense body, so consequently with high mechanical properties. However, the recovery time must be adapted to the size of the part and the printing speed in order to minimize the time needed to print a part. In our work, with a printing speed of 10 mm/s and a part size of 36 mm in length and 4 mm in width, it takes about 36 s to print a whole layer (10 filaments). As the recovery time of the ADPeg38 paste is longer than this value (it requires more than 100 s to recover 50% of the initial viscosity), its viscosity will still be low when the next layer is printed. Having a too long recovery time might lead to a collapse of the structure and thus a lack of geometrical fidelity.

Finally, a successfully printed ceramic part should present good functional properties (i.e. high strength in the present article). In order to obtain a functional part with homogeneous microstructure and good mechanical characteristics, it is necessary to avoid critical defects that could lead to failure. Thus, all the processing steps where the defects could originate from must be under control. Fig. 5A illustrates issues coming from the paste homogeneity: modifications of the mixing process described in the Ceramics paste preparation section, such as insufficient cooling and mixing time, may induce some aggregation of the PF127 and residual bubbles. Even with optimized paste preparation, although some printed parts may show no visible defects inside their body after a critical failure (Fig. 7), others show identifiable defects. Among them, the most critical seem to be the closest to the tensile surface, but also the large internal defects resulting from a lack of fusion between filaments. This kind of defects is found in the ADP42 bars (Fig. 8) (although in this case the surface morphology is more probably the origin of the failure). It is also observed by other authors (see for instance the Fig. 5 of Baltazar et al. [56]). These defects hardly impact the density, but they may be sufficiently large and acute to act as critical defects for the fracture. They may be avoided by fine-tuning the rheology as has been shown in the present article, together with optimizing the nozzle path.

To complement, one should also consider that the possibility of defects linked to debinding also points to the necessity of reducing the amounts of organics in the ceramic green body. Printing with PEG instead of the commonly used Pluronic is a good approach, since it allowed us to work with twice less organics. However, it should be possible to reduce even more the amount of organic materials, for instance by replacing PEG by gelatin or alginate (widely used in bioprinting by DIW [57-59]), or by using a completely different approach to get the right rheological properties, such as the dispersant-binder-coagulant approach, that uses minimal amounts of organics.

According to the previous paragraphs, Fig. 10 summarizes all the relevant parameters involved in the printing process of a ceramic part that this work has highlighted. This figure is not exhaustive and could be linked with the Fig. 9 of the relevant review from Lamnini et al. [60]. In our work, we consider that three successive levels of printability are required to achieve the desired part objectives: extrudability, shape fidelity and final performance. The first level, which indicates the ability of a

paste to continuously exit the nozzle, depends on the printer's force, the rheology of the paste and the external environment (mainly humidity and temperature in this case). This level actually provides the prerequisites for proper paste extrusion. The shape fidelity, which corresponds to the second level of printability, defines the fidelity of the desired shape of the part, i.e. the external shape and the internal design (dense or empty zone). To be correctly achieved, this level must take into account the complexity of the part. The parameters of the printer and the rheology of the paste must be adapted together. This optimization work, which involves many variables, requires the user's experience and many experiments to be carried out. As explained in our study, special attention must be paid to the recovery time, which influences both the external appearance and the correct connection of the filaments inside the body of the part. The last printability level concerns the final performance. Indeed, a part cannot be considered as 'printable' if it does not reach the required mechanical properties after the whole process. Therefore, sufficient mechanical properties are desired as final performance in our study. Thus, defects must be reduced, both on the surface of the part and inside the part. Defects, which usually originate from small, local initial heterogeneities, can then develop during all the processing steps of the ceramic, from drying to sintering, depending on their optimization. Thus, having a good shape fidelity, i.e. a smooth surface and a dense and homogeneous microstructure, is also of primary importance for good mechanical properties.

One should keep in mind that the definition of printability criteria is more advanced in the bioprinting field than in the ceramics field, and can encompass this idea of including the final function in the definition of the criteria. It is thus important to remember that the requisites for both fields are not all identical. Indeed, in particular the paramount functional requirement in bioprinting is to keep alive the cells contained in the paste, which leads to severe limitations in terms of the mechanical stresses to which cells are submitted, hence in terms of rheology of the paste. These demands cannot be translated in the ceramics field without adaptation. However, the idea of considering the final, desired properties as a part of the definition of printability criteria is common to the bioprinting field and to this article.

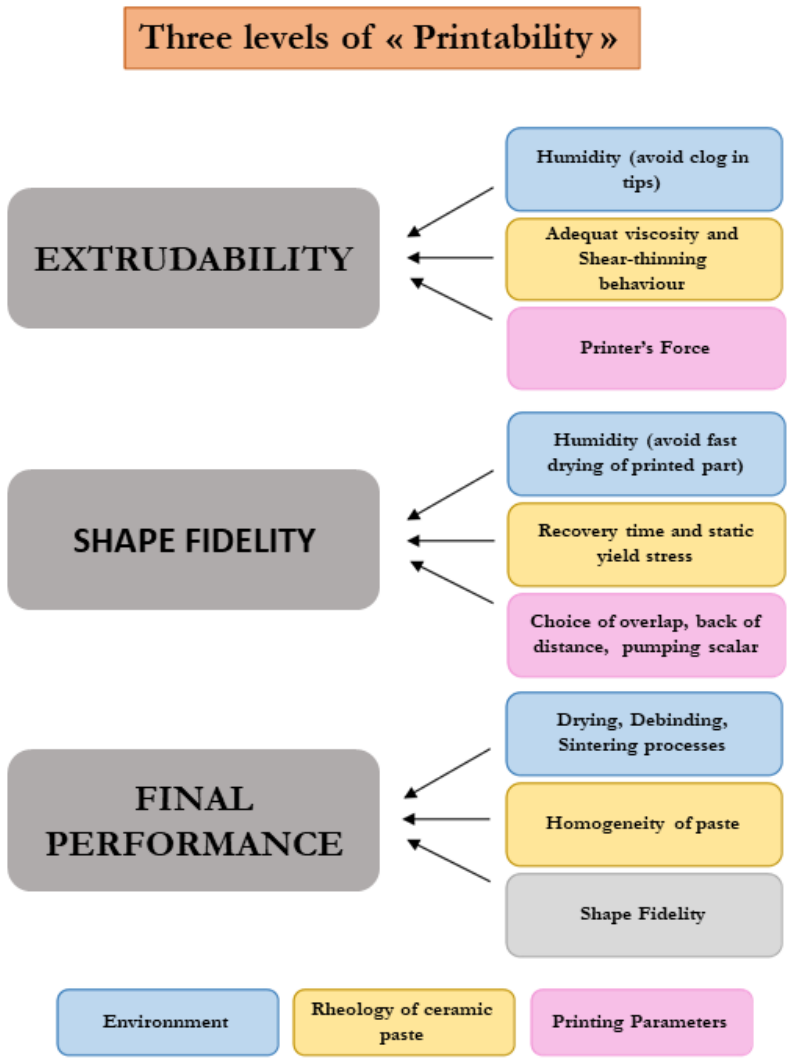

Figure 10. All parameters involved in the success of DIW of dense ceramic parts with satisfying mechanical properties.

The approach shown in the present paper enabled reaching good mechanical properties as compared to the literature: the strongest alumina shown here reach 350 MPa characteristic strength, with some samples resisting to 600 MPa, without polishing. This is 50% larger than previous results in the literature [27] and shows that further optimization may lead to robocast alumina parts with strength comparable to conventional processes. There are still issues with Weibull moduli obtained on ceramics made by additive manufacturing in general, showing a larger distribution of defects and thus a lower robustness than other more mature ceramic technologies. Weibull moduli obtained in this work, in line with previous literature [27], are a real point of vigilance for structural applications requiring low risk of failure. Reproducibility of additive manufactured ceramics should require further efforts. To go ahead in predicting the overall final performance of ceramic parts, machine learning, already applied to predict the mechanical properties of bio-ink [61,62], could be of great help in developing the pastes and printing conditions by reducing the time-consuming iterative process optimization.

6. Conclusion

Alumina printed parts were obtained by robocasting and exhibited in the best case characteristic flexural strength of about 350 MPa, which may be sufficient for several technical applications. It was necessary to optimize both rheological properties of the paste and printing parameters before reaching such fracture strength. In particular, and that might be counterintuitive for ceramists, pastes with the lower solid content reached the highest strength: this is due to their higher ability to flow and fill larger defects. Further optimization was obtained by exploiting the thixotropy: increasing the recovery time was proven to be beneficial to both surface roughness after printing and mechanical properties. Note that these results are linked to the rheology, not directly to the solid content: a better optimum might be reached for similar rheologies but higher solid content.

The optimization also concerned the formulation of the paste: even if Pluronic F127 is still among the most widely used gels to process ceramic pastes for direct ink writing, PEG can be an excellent substitute, enabling to fabricate pastes with similar rheological behavior, leading to a better shape fidelity, while facilitating debinding through the use of less organic material as compared to PF127.

Finally, during this work, three different kinds of rheological tests were performed to well define the printability, in order to obtain sufficient final mechanical properties without machining. The large set of rheological parameters illustrates why the ceramic community must be very precise in their definition and measurements, if only to avoid misunderstandings.

Declaration of Competing Interest

The authors declare that they have no known competing financial interests or personal relationships that could have appeared to influence the work reported in this paper.

Acknowledgments

This work was funded by the Agence Nationale de la Recherche (ANR) under ID ANR-17-CE08-0021, in the frame of CERAPIDE project. This work was performed in parallel with the work of Dr. Tristan Garnault, who we wish also to thank for his help in the assessment of the macroporosity.

References

1. S.M. Olhero, et al., Conventional versus additive manufacturing in the structural performance of dense alumina-zirconia ceramics: 20 years of research, challenges and future perspectives, J. Manuf. Process., 77 (2022), pp. 838-879
2. Z. Chen, et al., 3D printing of ceramics: A review, J. Eur. Ceram. Soc., 39 (2019), pp. 661-687
3. Women in 3D Printing, From Bones to Bridges and Everything in Between, Springer International Publishing, (2021), 10.1007/978-3-030-70736-1
4. E. Peng, D. Zhang, J. Ding, Ceramic robocasting: recent achievements, potential, and future developments, Adv. Mater., 30 (2018), Article 1802404
5. A. Zocca, et al., Additive manufacturing of ceramics: issues, potentialities, and opportunities, J. Am. Ceram. Soc., 98 (2015), pp. 1983-2001
6. Z. Chen, et al., Dense ceramics with complex shape fabricated by 3D printing: A review, J. Adv. Ceram., 10 (2021), pp. 195-218
7. Y. Lakhdar, C. Tuck, J. Binner, A. Terry, R. Goodridge, Additive manufacturing of advanced ceramic materials, Prog. Mater. Sci., 116 (2021), Article 100736
8. J.E. Smay, G.M. Gratson, R.F. Shepherd, J.C. Iii, J.A. Lewis, Directed Colloidal Assembly of 3D Periodic Structures, Adv. Mater., 5 (2002)
9. Gleadall, FullControl GCode Designer: Open-source software for unconstrained design in additive manufacturing, Addit. Manuf., 46 (2021), Article 102109
10. Gleadall, I. Ashcroft, J. Segal, VOLCO: A predictive model for 3D printed microarchitecture, Addit. Manuf., 21 (2018), pp. 605-618
11. S.S.L. Chan, M.L. Sesso, G.V. Franks, Direct ink writing of hierarchical porous alumina‐stabilized emulsions: Rheology and printability, J. Am. Ceram. Soc., 103 (2020), pp. 5554-5566
12. M'Barki, A. 3D Printed boehmite based objects. Material chemistry. Université de Lyon, 2018. English. 〈NNT: 2018LYSE1021〉. 〈tel-01973667〉
13. G. Ovarlez, Caractérisation rhéologique des fluides à seuil, Rhéologie, 20 (2011), pp. 28-43,
14. L. Del-Mazo-Barbara, M.-P. Ginebra, Rheological characterisation of ceramic inks for 3D direct ink writing: A review, J. Eur. Ceram. Soc., 41 (2021), pp. 18-33
15. E.-J. Courtial, et al., Silicone rheological behavior modification for 3D printing: Evaluation of yield stress impact on printed object properties, Addit. Manuf., 28 (2019), pp. 50-57
16. R.G. Larson, Y. Wei, A review of thixotropy and its rheological modelling, J. Rheol., 63 (2019), pp. 477-501
17. L. Tabard, et al., Robocasting of highly porous ceramics scaffolds with hierarchized porosity, Addit. Manuf., 38 (2021), Article 101776
18. Malvern Instruments Limited. A Basic Introduction to Rheology, 2016.
19. M. Champeau, et al., 4D printing of hydrogels: a review, Adv. Funct. Mater., 30 (2020), Article 1910606
20. Z. Fu, et al., Printability in extrusion bioprinting, Biofabrication, 13 (2021), Article 033001
21. L. Lemarié, A. Anandan, E. Petiot, C. Marquette, E.-J. Courtial, Rheology, simulation and data analysis toward bioprinting cell viability awareness, Bioprinting, 21 (2021), Article e00119
22. A.Lopez, C.A. Marquette, E.-J. Courtial, FingerMap: a new approach to predict soft material 3D objects printability, Prog. Addit. Manuf., 6 (2021), pp. 53-62
23. M'Barki A. et al. Linking Rheology and Printability for Dense and Strong Ceramics by Direct Ink Writing. Scientific REPOrtS 10.
24. S. Naghieh, X. Chen, Printability–A key issue in extrusion-based bioprinting, J. Pharm. Anal., 11 (2021), pp. 564-579
25. Schwab, et al., Printability and Shape Fidelity of Bioinks in 3D Bioprinting, Chem. Rev., 120 (2020), pp. 11028-11055
26. E. Feilden, et al., 3D printing bioinspired ceramic composites, Sci. Rep., 7 (2017), p. 13759
27. E. Feilden, E.G.-T. Blanca, F. Giuliani, E. Saiz, L. Vandeperre, Robocasting of structural ceramic parts with hydrogel inks, J. Eur. Ceram. Soc., 36 (2016), pp. 2525-2533

28. A. Neto, J. Ferreira, Synthetic and marine-derived porous scaffolds for bone tissue engineering, Materials, 11 (2018), p. 1702
29. Corker, H.C.-H. Ng, R.J. Poole, E. García-Tuñón, 3D printing with 2D colloids: designing rheology protocols to predict 'printability' of soft-materials, Soft Matter, 15 (2019), pp. 1444-1456
30. M. Dinkgreve, J. Paredes, M.M. Denn, D. Bonn, On different ways of measuring "the" yield stress, J. Non-Newton. Fluid Mech., 238 (2016), pp. 233-241
31. P. Coussot, Q.D. Nguyen, H.T. Huynh, D. Bonn, Avalanche behavior in yield stress fluids, Phys. Rev. Lett., 88 (2002), Article 175501
32. Chen, T. Rheological Techniques for Yield Stress Analysis. On-Line document from TA Instruments, New Castle, Delaware, USA. https://www.tainstruments.com/pdf/literature.
33. J.A. Lewis, Direct Ink Writing of 3D Functional Materials, Adv. Funct. Mater., 16 (2006), pp. 2193-2204
34. J.A. Lewis, Colloidal processing of ceramics, J. Am. Ceram. Soc., 83 (2004), pp. 2341-2359
35. J.E. Smay, J. Cesarano, J.A. Lewis, Colloidal Inks for Directed Assembly of 3-D Periodic Structures, Langmuir, 18 (2002), pp. 5429-5437
36. J. Mewis, Thixotropy - a general review, J. Non-Newton. Fluid Mech., 6 (1979), pp. 1-20
37. J. Mewis, N.J. Wagner, Thixotropy, Adv. Colloid Interface Sci., 147–148 (2009), pp. 214-227
38. Feilden, E. Additive Manufacturing of Ceramics and Ceramic Composites via Robocasting. (Imperial College London, 2017). doi:10.13140/RG.2.2.29343.25765.
39. Tabard, L. Elaboration de céramiques architecturées pour le stockage d'énergie thermique. Material Chemistry. PhD thesis Université de Lyon. 〈NNT2020LYSEI007〉, 198 pages, 2020.
40. M. Lorenz, et al., Influence of platelet content on the fabrication of colloidal gels for robocasting: Experimental analysis and numerical simulation, J. Eur. Ceram. Soc., 40 (2020), pp. 811-825
41. T. Trincat, et al., Influence of the printing process on the traces produced by the discharge of 3D-printed Liberators, Forensic Sci. Int., 331 (2022), Article 111144
42. J. Allum, A. Moetazedian, A. Gleadall, V.V. Silberschmidt, Interlayer bonding has bulk-material strength in extrusion additive manufacturing: New understanding of anisotropy, Addit. Manuf., 34 (2020), Article 101297
43. G. Franchin, et al., Optimization and Characterization of Preceramic Inks for Direct InkWriting of Ceramic Matrix Composite Structures, Materials, 11 (2018), p. 515
44. Garnault, T. Frittage par micro-ondes de céramiques mises en forme par impression 3D. Génie des procédés. Université Grenoble Alpes, 2020. Français. NNT: 2020GRALI077. tel-03166743
45. Hugonnet B. Frittage et évolution de la microstructure au cours des traitements thermiques d' aimants NdFeB: influence sur les propriétés magnétiques. Electromagnétisme. Université Grenoble Alpes, 2016. Français. NNT: 2016GREAI079. tel-01689768.
46. W. Li, J. Sun, Effects of Ceramic Density and Sintering Temperature on the Mechanical Properties of a Novel Polymer-Infiltrated Ceramic-Network Zirconia Dental Restorative (Filling) Material, Med Sci. Monit., 24 (2018), pp. 3068-3076
47. Camposilvan, E., Surface stability and small‐scale testing of zirconia. Universitat Politècnica de Catalunya. PhD thesis Departament de Ciència dels Materials i Enginyeria Metallúrgica, 2015, 146 pages.
48. Y. Chen, et al., A novel thixotropic magnesium phosphate-based bioink with excellent printability for application in 3D printing, J. Mater. Chem. B, 6 (2018), pp. 4502-4513
49. G. de With, Note on the use of the diametral compression test for the strength measurement of ceramics, J. Mater. Sci. Lett., 3 (1984), pp. 1000-1002
50. I.J. Davies, Confidence limits for Weibull parameters estimated using linear least squares analysis, J. Eur. Ceram. Soc., 37 (2017), pp. 5057-5064
51. R. Morrell, Fractography and fracture toughness measurement, KEM, 409 (2009), pp. 17-27
52. Cai, Q. et al., 3d-Printing of Ceramic Filaments with Ductile Metallic Cores. Available at SSRN: https://ssrn.com/abstract=4241487.

53. ISO 6872. Dentistry – ceramic materials. Geneva: International Organization for Standardization; 2008.
54. Altay, M.A. Gülgün, Microstructural evolution of calcium-doped α-alumina, J. Am. Ceram. Soc., 86 (2003), pp. 623-629
55. S.N. Heavens, Structural transformation during sintering and annealing of beta alumina, J. Mater. Sci., 19 (1984), pp. 2223-2232
56. J. Baltazar, et al., Influence of filament patterning in structural properties of dense alumina ceramics printed by robocasting, J. Manuf. Process., 68 (2021), pp. 569-582
57. E. Axpe, M. Oyen, Applications of Alginate-Based Bioinks in 3D Bioprinting, IJMS, 17 (2016), p. 1976
58. Q. Gao, B.-S. Kim, G. Gao, Advanced Strategies for 3D Bioprinting of Tissue and Organ Analogs Using Alginate Hydrogel Bioinks, Mar. Drugs, 19 (2021), p. 708
59. T. Gao, et al., Optimization of gelatin–alginate composite bioink printability using rheological parameters: a systematic approach, Biofabrication, 10 (2018), Article 034106
60. S. Lamnini, et al., Robocasting of advanced ceramics: ink optimization and protocol to predict the printing parameters - A review, Heliyon, 8 (2022), Article e10651
61. G.D. Goh, S.L. Sing, W.Y. Yeong, A review on machine learning in 3D printing: applications, potential, and challenges, Artif. Intell. Rev., 54 (2021), pp. 63-94
62. J. Lee, S.J. Oh, S.H. An, W.-D. Kim, S.-H. Kim, Machine learning-based design strategy for 3D printable bioink: elastic modulus and yield stress determine printability, Biofabrication, 12 (2020), Article 035018